

# Calculation of ionization and total and partial charge exchange cross sections for collisions of $C^{6+}$ and $N^{7+}$ with H

Alba Jorge, L.F. Errea, Clara Illescas and L. Méndez

Laboratorio Asociado al CIEMAT de Física Atómica y Molecular en Plasmas de Fusión.

Departamento de Química, módulo 13, Universidad Autónoma de Madrid, Cantoblanco E-28049 Madrid, Spain.

e-mail: alba.jorge@uam.es

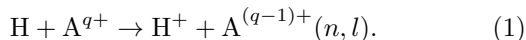
Received: date / Revised version: date

**Abstract.** We have performed calculations for collisions between fully stripped ions,  $C^{6+}$  and  $N^{7+}$ , and atomic hydrogen, in both its ground and first excited energy levels. We have employed the Classical Trajectory Monte Carlo method to obtain total ionization and charge exchange cross sections and state selective charge exchange cross sections in the 5-500 keV/amu energy range.

**PACS.** a hh+00 34.70.+e – 34.10.+x

## 1 Introduction

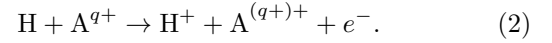
Charge exchange (CX) between fully stripped ions and Hydrogen atoms is a main subject of interest in fusion research, since cross sections for these processes are needed in different fields [1], particularly in Charge eXchange Recombination Spectroscopy (CXRS) [2]. CXRS is a reliable diagnostic tool to determine ion temperature, impurity density and charge state of the impurities in fusion plasmas and it is present in most fusion devices (see e.g. [3] for a review on active spectroscopy techniques for plasma diagnostics). The CXRS diagnostic is based on the injection of a beam, usually of D atoms. The injected atoms collide with the plasma ions giving rise to CX (also called electron capture) reactions. In particular, the collisions with the impurity ions  $A^{q+}$  lead to the reactions:



The beam atoms have energies larger than 20 keV/amu. At these energies, the isotopic dependence of the cross sections of reactions (1) is negligible and accordingly we

have employed the symbol H in (1) to indicate any Hydrogen isotope. Reaction (1) leads to ions  $A^{(q-1)+}$  in excited states, which decay radiatively; the analysis of the ensuing emission provides the above-mentioned plasma parameters. The fundamental atomic data required in CXRS are  $nl$ -state-selective cross sections, where  $n$  and  $l$  are the quantum numbers of the orbital populated after the reaction; these data are required in the collisional-radiative model, which yields the effective emission coefficients needed in the diagnostics. In this respect, The Atomic Data and Analysis Structure (ADAS) [4, 5] database stores the required atomic data and has implemented the collisional-radiative model to compute the effective emission coefficients.

The intensity of the light emitted in the CXRS diagnostics depends on the neutral beam density, which is reduced by the ionization reactions:



In practice, the H density is obtained numerically through the application of a collisional-radiative model to determine the attenuation of the neutral beam. Alternatively, the CXRS measurements can be combined with beam emission spectroscopy, and in both cases ionization cross sections are required.

In the present work, we study collisions of medium-charged ions  $A^{q+} = C^{6+}, N^{7+}$  with hydrogen atoms with the aim of obtaining state-selective cross sections and of providing scaling laws, useful to extrapolate the results to highly-charged projectiles, such as Tungsten ions, relevant to plasma diagnostics in ITER [6]. In general, as the impurity charge,  $q$ , increases, the study of CX reactions becomes more difficult, both theoretical and experimentally, and a proper scaling law, derived from calculations for collisions with low- $q$  ions is desirable. Previous works [7–9] have already suggested scaling rules for total and partial CX cross sections and, in particular, Foster [9] has proposed an universal parametric curve, based on data for low/intermediate  $q$  ions to extrapolate them to collisions with highly ionized projectiles [10]. One objective of the present work is to check the validity of the universal curve in the collisions of  $C^{6+}, N^{7+}$  with  $H(n=1,2)$ .

With respect to the relevance of the particular ions studied in this paper, Carbon has been widely used as a material of the plasma facing components, but future fusion devices will dismiss carbon as a plasma facing material because it traps large quantities of Tritium by codeposition and it will be substituted by high- $q$  species like Tungsten. Nevertheless,  $C^{6+}$  is an expected impurity in ITER, where it will be used in spectroscopic diagnostics [11]. On the other hand, the injection of some elements intentionally (impurity seeding) reduces the peak power load on the divertor, and different species, such as Ne or Ar [12], are under research to convert heat flux into radiation. Nitrogen is also a proper extrinsic radiator to cool the plasma edge, and  $N_2$  seeding has become a routine tool in the ASDEX tokamak [13]; obviously, this will lead to the presence of fully stripped Nitrogen ions in the core plasma.

The diagnostic neutral beam is mainly formed by atoms in the ground state. Nevertheless, it can contain atoms in  $n = 2$ , and also a small proportion of atoms can be excited in collisions with the plasma particles [14, 15]. Experimental cross sections for electron capture and ionization in collisions with excited hydrogen are not available, and there is a need of theoretical calculations to obtain these cross sections, especially due to the fact that CX cross sections for collisions with  $H(n=2)$  are one order of magnitude greater than those with  $H(1s)$  at  $E \approx 40 \text{ keV/amu}$ , which can lead to sizeable values of the corresponding effective emission coefficients [16, 17]. For the particular case of the  $8 \rightarrow 7$  line of  $C^{5+}$ , it has been estimated [18] that, in a Deuterium plasma with densities  $N_e = N_i = 10^{14} \text{ cm}^{-3}$  and temperatures  $T_e = T_i = 15 \text{ keV}$ , the effective emission coefficient for collisions with a 100 keV  $H(n=2)$  beam is  $0.29 \times 10^{-14} \text{ m}^3/\text{s}$ , while the corresponding one for collisions with  $H(1s)$  is  $0.47 \times 10^{-14} \text{ m}^3/\text{s}$ .

Previous calculations for collisions of  $C^{6+}$  and  $N^{7+}$  with  $H(1s)$  have been carried out using semiclassical close-coupling methods with molecular (MOCC) [19] and atomic (AOCC) [20, 21] bases, the Classical Trajectory Monte Carlo method (CTMC) [22, 23], continuum-distorted-wave (CDW-EIS) methods [24, 25] and the eikonal impulse approximation (EI) [26]. The AOCC and CTMC calculations of Igenbergs and coworkers [21] show marked differences in both total and state selective CX cross sections at low collision energies, and considerable deviations are also observed in the ionization cross sections. In the energy region of the ITER CXRS beam [27],  $E \approx 100 \text{ keV/amu}$ , ionization, electron capture and excitation are competitive processes, and the application of close-coupling methods requires the use of very large basis sets with pseudostates. However, it has been shown that the CTMC method [28, 23, 29] provides reliable total cross sections for all processes at  $E \gtrsim 15 \text{ keV/amu}$ . In particular, the use of improved initial distributions has allowed to evaluate state selective CX cross sections for several systems [30–33], which have been merged with semiclassical calculations to provide sets of recommended data. This method has been recently applied to calculate excitation cross sections in [34]. The CTMC method has also been applied to study collisions with excited atoms (e.g. [16, 33, 21, 35, 36]).

The aim of this work is firstly to study the differences of charge exchange cross sections at low energies in [21] and secondly, to recommend accurate ionization cross sections for collisions with  $H(n = 1, 2)$ , which are of interest for the beam penetration into the plasma [37, 38]. The calculations have been carried out by employing a CTMC method with improved initial distributions. Preliminary results on these collisions were presented at the HCI Conference [39].

The paper is organized as follows: In section 2, we briefly outline the CTMC method. In section 3 we present our results followed by some conclusions in section 4. Atomic units ( $\hbar = 1, e = 1, m_e = 1$ ) are used unless otherwise stated.

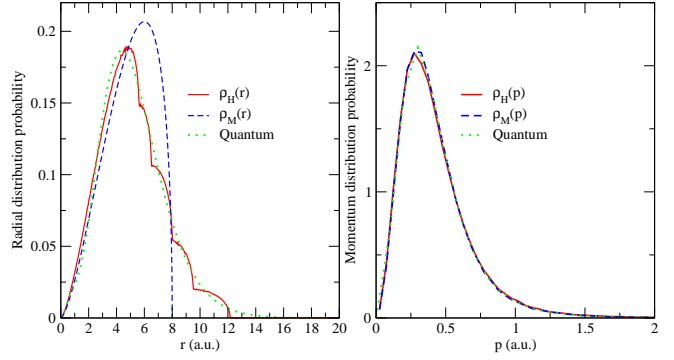


**Fig. 1.** Comparison of classical, microcanonical ( $\rho_M$ ) and hydrogenic ( $\rho_H$ ), and quantum distribution of  $H(n=2)$

## 2 Theoretical method

We use the Classical Trajectory Monte Carlo method [28] under the impact-parameter approximation [40], in which  $\mathbf{R}$ , the internuclear position vector follows linear trajectories  $\mathbf{R} = \mathbf{v}t + \mathbf{b}$ , with relative nuclear velocity  $\mathbf{v}$  and impact parameter  $\mathbf{b}$ . The electronic motion is described classically by using a statistical collective of  $N$  ( $N = 2 \times 10^5$ , in our calculations) non-interacting particles:

$$\rho(\mathbf{r}, \mathbf{p}, t) = \frac{1}{N} \sum_{j=1}^N \delta(\mathbf{r} - \mathbf{r}_j(t)) \delta(\mathbf{p} - \mathbf{p}_j(t)) \quad (3)$$

which must satisfy the Liouville equation for the fixed-nuclei Born-Oppenheimer electronic Hamiltonian. The electron trajectories  $\{\mathbf{r}_j(t), \mathbf{p}_j(t)\}$  are solutions of the Hamilton's equations for the electron motion in the two-center Coulomb potential.

The accuracy of the CTMC method strongly relies on the choice of the initial distribution. This method is commonly applied using the so-called microcanonical distribution [28, 41–43, 21], in which all electron trajectories have the same energy,  $\epsilon$ . As it is well-known, (e.g. [22]), this classical description of the  $H(1s)$  orbital implies a cut-off of the spatial distribution at  $r_0 = 2 \text{ a.u.}$  Similarly, the  $H(n=2)$  spatial distribution shows a cut-off at  $r_0 = 8 \text{ a.u.}$ , as shown in Fig 1; the tail of the quantal distribution for  $r > r_0$ , correspond to classically forbidden trajectories.

Several works [22, 44, 45, 29] have suggested alternative initial distributions, where the radial distribution fits the quantal one. In this respect, the study of reference [29], showed that all these distributions yield practically identical results. In particular, Hardie and Olson [22] proposed the use of an initial distribution, the so-called hydrogenic distribution, which is formed by a superposition of eight microcanonical distributions with different energies, whose weights,  $a_j$ , were calculated so as to fit the spatial quantal density together with the condition:  $\langle \epsilon \rangle = \sum_{j=1}^m a_j \epsilon_j = \epsilon$ . In this work, we have employed a combination of ten microcanonical distributions for the description of the ground state  $H(1s)$  [23] and six for the excited state  $H(n = 2)$ , to better describe the quantum radial densities. The initial microcanonical and hydrogenic

distributions are compared to the quantal ones in Fig. 1 for  $H(n=2)$ , where it can be noted that the use of the hydrogenic distribution clearly improves the description of the microcanonical spatial distribution without significantly modify the momentum distribution. Similar comparisons for  $H(n=1)$  can be found in reference [29]. Previous calculations on  $Li^{3+}$ ,  $B^{5+}$  and  $Ne^{10+} + H$  collisions [30,29,33] showed that the hydrogenic-CTMC treatment provides accurate ionization and total and  $n$ -resolved electron capture cross sections for  $n \gtrsim n_{\max}$ , where  $n_{\max}$  is the most populated level of the ion  $A^{(q-1)+}$  formed in the CX reaction. The microcanonical-CTMC treatment leads in general to more accurate CX cross sections into low-lying states, as explained in detail in [29]. It must be pointed out that generally transitions in the visible spectrum, those of interest in CXRS, take place from energy levels with  $n > n_{\max}$ . With regard to the ionization process, the use of a hydrogenic-CTMC treatment shows a clear improvement respect to the standard microcanonical-CTMC cross sections, in the case of collisions with  $H(1s)$ , in particular, at the threshold region [46,23,47].

Once the initial distribution is constructed, the Hamilton equations are integrated for each nuclear trajectory  $\mathbf{R}(t)$  until the final time of integration,  $t_{\max} = 500v^{-1}$ , for which the cross sections have converged. In order to evaluate transition probabilities and cross sections we apply the energy criteria in which ionization takes place if  $E_T, E_P > 0$  and electron capture does if  $E_P < 0$  ( $E_T, E_P$  are the electron energies with respect to the target and projectile at  $t = t_{\max}$ , respectively). The corresponding ionization and electron capture probabilities are evaluated from the asymptotic values of the distribution functions,  $\rho^i$  and  $\rho^c$ ,

$$P_{i,c}(v, b) = \int d\mathbf{r} \int d\mathbf{p} \rho^{i,c}(\mathbf{r}, \mathbf{p}; v, b, t_{\max}) \quad (4)$$

Total cross sections are then calculated by integrating the transition probabilities over the impact parameter:

$$\sigma_{i,c} = 2\pi \int_{b_{\min}}^{b_{\max}} db b P_{i,c}(v, b) \quad (5)$$

where  $b_{\min} = 0$  and  $b_{\max}$  varies depending of the process, the collisional target and the collision velocity. For collisions with  $H(1s)$ ,  $b_{\max} \approx 20$  a.u. and, for collisions with  $H(n = 2)$  targets,  $b_{\max} \approx 20$  a.u. for capture and  $b_{\max} \approx 54$  a.u. for ionization. In order to obtain CX  $n$ - and  $nl$ - resolved cross sections, those associated to the quantum numbers  $n$  and  $l$  of the electron bound states after CX, we have applied the Becker and Mackellar (BM) method [42,48]. They proposed to partition the phase space into adjacent and non-overlapping “bins”, each of them associated with a quantum number  $n$  and  $l$ . A given electron trajectory belongs to the bin associated to the quantum state  $nl$  if fulfills:

$$n \left( n - \frac{1}{2} \right) (n - 1) \leq n_c^3 < n \left( n + \frac{1}{2} \right) (n + 1) \quad (6)$$

and

$$l \leq \frac{n}{n_c} L_c < l + 1, \quad (7)$$

where

$$n_c = \frac{Z_P}{\sqrt{-2E_P}}; \quad \mathbf{L}_c = \mathbf{r}_P \times \mathbf{p}_P \quad (8)$$

being  $\mathbf{r}_P = \mathbf{r} - \mathbf{b}$  and  $\mathbf{p}_P = \mathbf{p} - \mathbf{v}$  the electron position and momentum respect to the projectile. Thus, the capture density  $\rho^c$  is divided into  $\rho_n^c$  and in turn in  $\rho_{nl}^c$  by including the trajectories in the corresponding boxes. State-selective probabilities and cross sections are determined by replacing  $\rho^c$  by  $\rho_n^c$  or  $\rho_{nl}^c$  in (4) and (5).

### 3 Results

#### 3.1 Total cross sections: Collisions with $H(1s)$

Total charge exchange cross sections for  $C^{6+} + H(1s)$  collisions are displayed in Fig. 2. We have plotted our data obtained using both, microcanonical and hydrogenic initial distributions, compared to the existing experimental data and previous calculations. At low energies,  $E < 40$  keV/amu, we observe that computed microcanonical cross sections are lower than those obtained using an hydrogenic distribution, which are close to the measurements by Meyer *et al.* [49] and show a very good agreement with the MOCC calculations from Harel *et al.* [19] and with two sets of AOCC calculations from Toshima [20] and Igenbergs *et al.* [21]. At  $E > 150$  keV/amu, both classical calculations yield indistinguishable results, they correctly describe the fast decrease of the total cross section and agree with the experimental data of Goffe *et al.* [50], first-Born calculations of Belkić *et al.* [25] and EI calculations of Gravielle *et al.* [26]. With respect to the comparison between different CTMC calculations, our total cross sections obtained with the microcanonical distribution, are indistinguishable from those reported in reference [21], and those calculated with the hydrogenic distribution are identical to the previous calculations of references [22, 23], not shown in Fig. 2. The ADAS database contains interpolated data from references [51–53] which are lower than the present hydrogenic results and the AOCC cross sections [21] by about 15-20% at  $20 \leq E \leq 80$  keV/amu.

We compare in Fig. 3 our CX total cross sections for  $N^{7+} + H(1s)$  collisions to low energy measurements of Meyer *et al.* [49], which are close to our hydrogenic classical results, also in very good agreement with the MOCC results from Harel *et al.* [19] and with the AOCC data of references [20,21]. The cross section stored in ADAS for  $N^{7+} + H(1s)$  were obtained by interpolation of those for  $C^{6+}$  and  $O^{8+}$  projectiles and do not agree with the present CTMC cross sections.

The ionization cross sections for  $C^{6+}$  and  $N^{7+} + H(1s)$  collisions are displayed in Fig. 4. In contrast with the results for CX, the corresponding microcanonical and hydrogenic ionization cross sections do not coalesce even at the highest energy shown in the figure. For  $C^{6+} + H(1s)$  collisions, the hydrogenic-CTMC results (the present ones and those of reference [22]) agree with the AOCC results of Toshima [20]; however, the recent AOCC calculations of Igenbergs *et al.* [21] show better agreement with

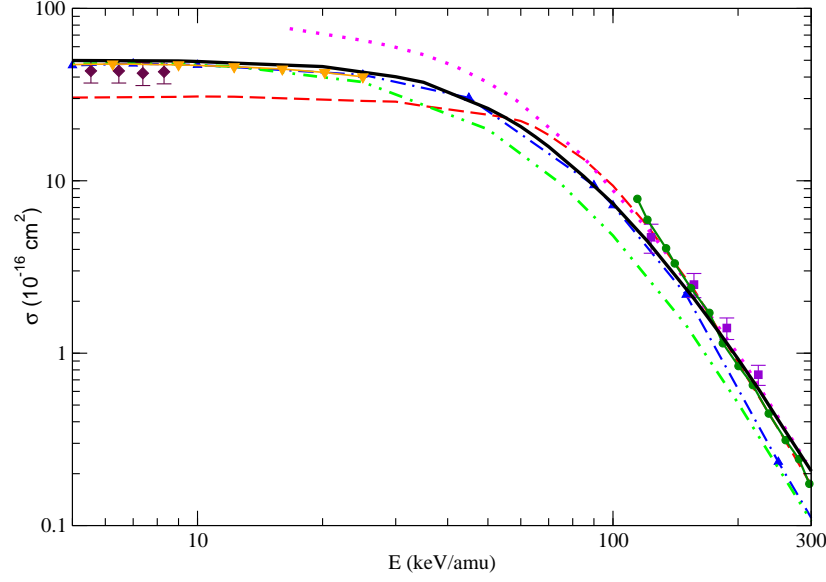


**Fig. 2.** Total charge exchange cross sections in  $C^{6+} + H(1s)$  collisions. Present calculations: (—) hydrogenic-CTMC; (---) microcanonical-CTMC; ( $\blacktriangle$ — $\blacktriangle$ ) AOCC [21]; ( $\bullet$ — $\bullet$ ) EI [26]; (— · —) AOCC [20]; ( $\cdot$  ·  $\cdot$ ) First Born approximation [25]; ( $\blacktriangledown$ — $\blacktriangledown$ ) MOCC [19]; and experimental: ( $\blacklozenge$ ) Meyer *et al.* [49]; ( $\blacksquare$ ) Goffe *et al.* [50].

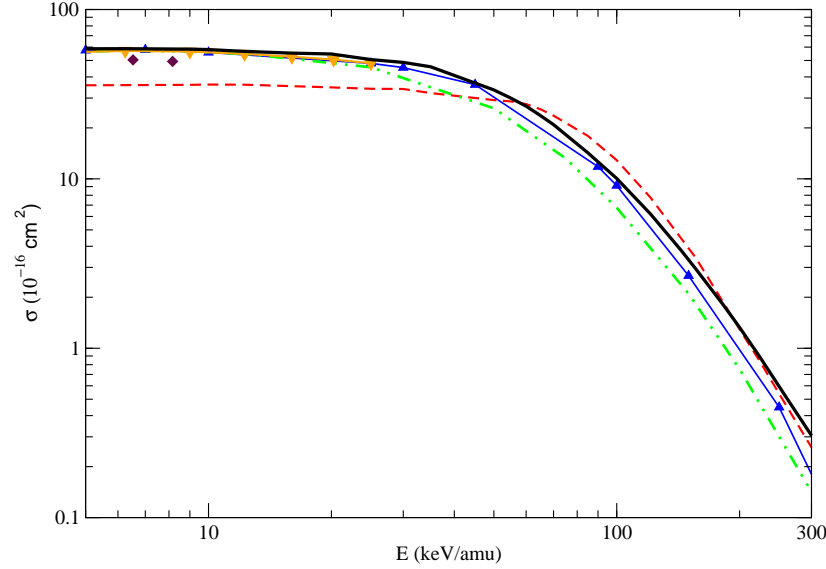


**Fig. 3.** Total charge exchange cross sections in  $N^{7+} + H(1s)$  collisions. Present calculations: (—) hydrogenic-CTMC; (---) microcanonical-CTMC; ( $\blacktriangle$ — $\blacktriangle$ ) AOCC [21]; (— · —) AOCC [20]; ( $\blacktriangledown$ — $\blacktriangledown$ ) Molecular calculations from Harel *et al.* [19]; and experimental: ( $\blacklozenge$ ) Meyer *et al.* [49].

our microcanonical-CTMC ionization cross sections. The comparison of the cross sections for  $N^{7+}$  projectiles of in Fig. 4b. shows that both semiclassical AOCC sets of results [20,21] better agree with our hydrogenic-CTMC cross section. Previous calculations [22,46,54,23,47,55] have clearly shown that the hydrogenic initial distribution yields accurate ionization cross sections. In this respect, the cut-off of the microcanonical distribution precludes to accurately evaluate ionization cross sections, and the agreement of the microcanonical result with the AOCC ioniza-

tion cross sections of reference [21] is fortuitous; the underestimation of the ionization cross section in the AOCC calculation of reference [21] may be a consequence of the fact that the number of unbound orbitals, all centered in the H nucleus, included in the expansion for  $C^{6+} + H$  collisions, is noticeably lower than the corresponding number employed for the description of the  $N^{7+} + H$  collisions (34 and 63 respectively). On the other hand, the basis set of reference [20] included a large set Gaussian-type orbitals centered in both nuclei to provide a good repre-

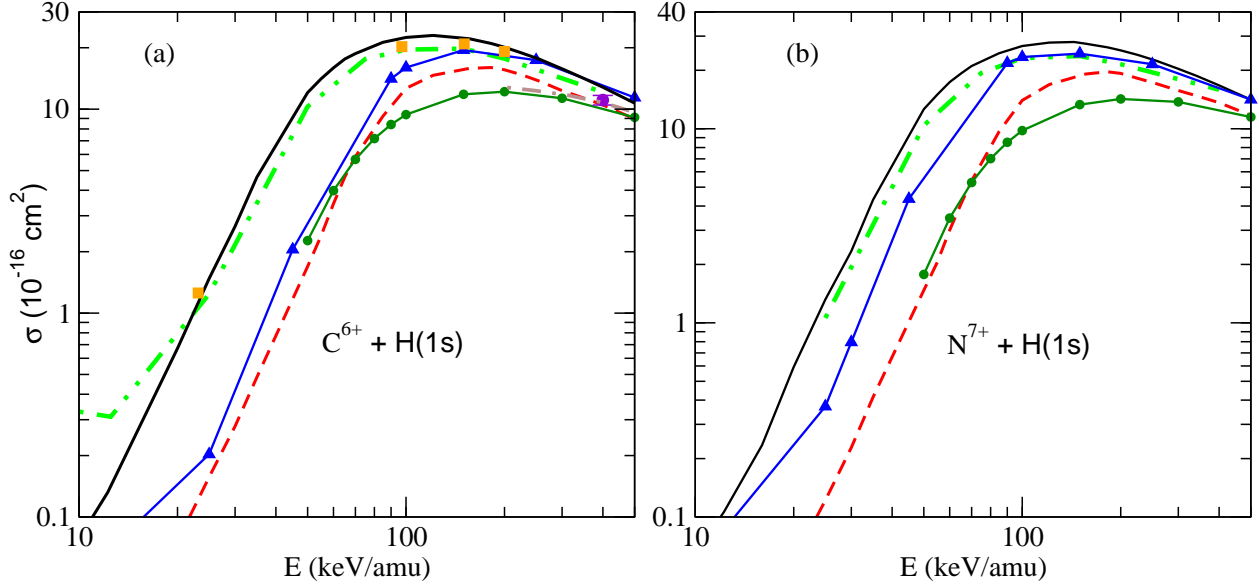


**Fig. 4.** Ionization cross sections for  $C^{6+}+H(1s)$  (a) and  $N^{7+}+H(1s)$  (b) collisions. (—) hydrogenic-CTMC; (---) microcanonical-CTMC; (■) hydrogenic-CTMC results of Hardie and Olson [22]; (▲—▲) AOCC [21]; (— · —) AOCC [20]; (●—●) CDW-EIS [24].

sensation of continuum states with the aim of obtaining accurate ionization cross sections, while the calculation of reference [21] was focused on modelling the CX process. Therefore, we expect more accurate ionization cross sections from reference [20], which better agrees with our hydrogenic-CTMC ionization cross sections. The CDW-EIS ionization cross sections from [24], also included in Fig. 4, underestimates the cross section at the energies shown in this figure.

### 3.2 Total cross sections: Collisions with $H(n=2)$

In this section we present our total charge exchange and ionization cross sections for  $C^{6+}$  and  $N^{7+}$  projectiles in collision with  $H(n=2)$ . Since there are not any experiment, we have compared our results for these collisions with the calculation of reference [21] (see Figs. 5 and 6).

It is worth noting that in the case of excited  $H(n=2)$  targets, both classical calculations, microcanonical and hydrogenic, lead to similar total CX cross sections, and in good agreement with the semiclassical results from reference [21] in the whole energy range considered in this work. We must point out that the CTMC microcanonical cross sections from [21] are identical to those obtained in this work, and also identical to those stored in ADAS (for  $C^{6+}$  collisions and  $5 < E < 50$  keV/amu) [16], so we have plotted only our data for clarity. With respect to the ionization cross section, we observe differences between the microcanonical and hydrogenic results in the threshold region that disappear for  $E \gtrsim 30$  keV/amu. The disagreement with the AOCC ionization cross section observed in Fig. 5 is less pronounced in  $N^{7+} + H(n=2)$  collisions (see Fig. 6) as previously found for collisions with

$H(1s)$ . This behaviour reinforces the argument that the AOCC basis set is poor for describing the continuum of the  $CH^{6+}$  system, yielding small ionization cross sections, while the relatively larger set of pseudostates allowed them to improve the description of the  $NH^{7+}$  continuum.

In the classical description of the  $H(n=2)$  target, we find an abrupt decrease of the spatial microcanonical initial distribution with respect to the quantal one (Fig. 1), although its effect on the collision transition probabilities is considerably less noticeable than for collisions with the  $H(1s)$  target, probably because the greater extension of the radial density [33]. In order to further illustrate this fact, we compare in Fig. 7 the charge exchange and ionization transition probabilities for  $C^{6+} + H(n=2)$  collisions, calculated using microcanonical and hydrogenic initial distributions for  $E = 20$  and 50 keV/amu; in general, both calculations lead to similar  $bP(b)$  values, and therefore, similar total cross sections. However, the cut-off in the radial microcanonical distribution limits the range of impact parameters where the ionization process takes place in the threshold region ( $E \approx 20$  keV/amu).

### 3.3 Partial $n$ -resolved cross sections

In this section we present our  $n$ -resolved CX cross sections. We are mainly interested in the populations of the levels near  $n=7-9$  because the transitions  $n_i = 8 \rightarrow n_f = 7$  ( $C^{5+}$ ) and  $n_i = 9 \rightarrow n_f = 8$  ( $N^{6+}$ ) lie in the visible spectrum and therefore are of interest in CXRS diagnostics.

Fig. 8 shows our CTMC partial cross sections for collisions with the  $H(1s)$  target compared with the semiclassical AOCC [21] and MOCC [19] results. In general, we find a very good agreement for both collisional systems

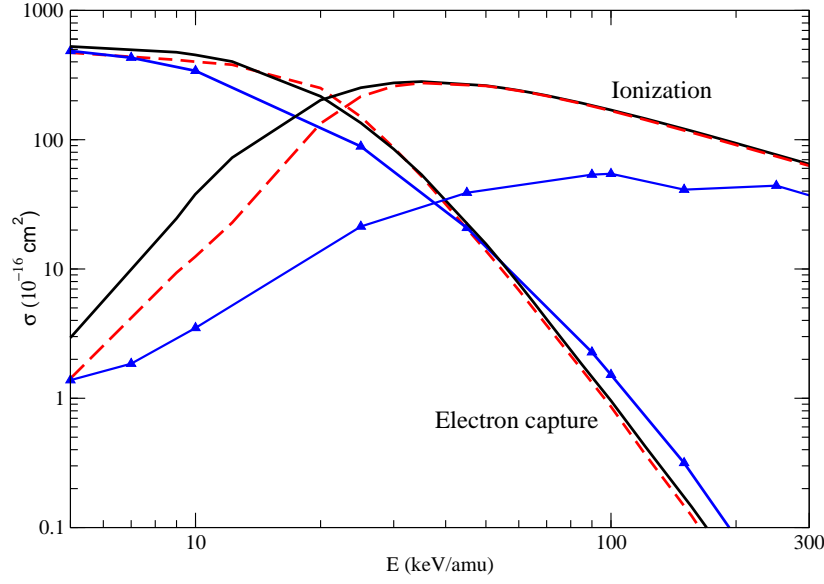


**Fig. 5.** Total charge exchange and ionization cross sections for  $C^{6+} + H(n=2)$  collisions: (—) hydrogenic-CTMC; (---) microcanonical-CTMC and ( $\blacktriangle$ — $\blacktriangle$ ) AOCC results from Igenbergs *et al.* [21].

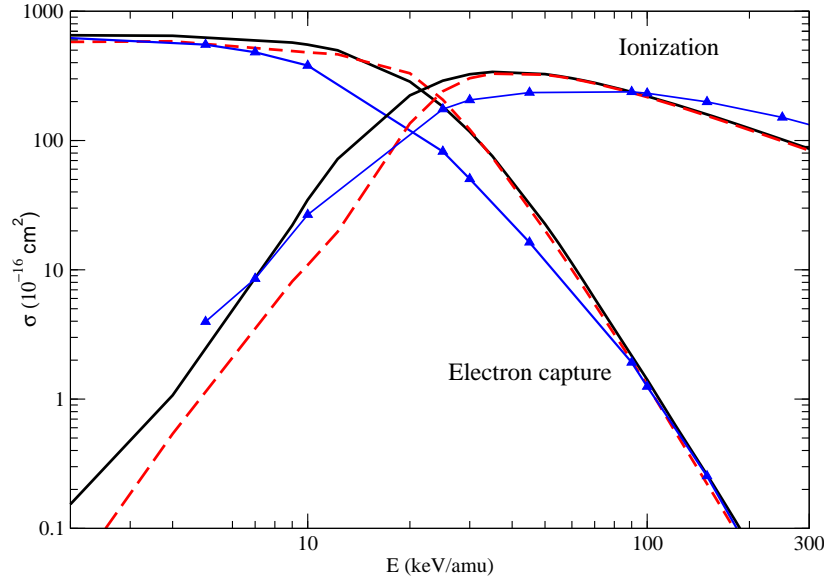


**Fig. 6.** Total charge exchange and ionization cross sections for  $N^{7+} + H(n=2)$  collisions: (—) hydrogenic-CTMC; (---) microcanonical-CTMC and ( $\blacktriangle$ — $\blacktriangle$ ) AOCC results from Igenbergs *et al.* [21].

although at low impact energies,  $E \leq 40$  keV/amu, the agreement worsens as  $n$  increases. For the lowest  $n$  levels shown in Fig. 8, the microcanonical CTMC partial cross sections agree with the semiclassical data, but, as the collision energy increases the microcanonical cross sections show an unphysical rapid fall as  $n$  increases, as it was found in previous works [29–31, 33].

We have plotted in Fig. 9 our hydrogenic-CTMC  $n$ -resolved partial cross sections for  $C^{6+}$ ,  $N^{7+} + H(n=2)$  collisions, for those levels decaying in the visible spectrum that incidentally are the largest  $n$ -partial cross sections. It can be noted that these cross sections drop off very fast,

almost three orders of magnitude from 10 to 100 keV/amu. AOCC results from [21] are also plotted and we find a very good agreement throughout the energy range of Fig. 9, only at  $E > 100$  keV/amu AOCC data show an overestimation compared to the classical cross sections, this effect is more prominent at the highest  $n$  level, and we believe that, at these energies, the CTMC calculation provides a better description of the electron capture into high  $n$ , since the AOCC calculation begins to undergo basis limitations, which are more severe in the case of  $C^{6+}$  projectiles, see Fig. 9. This effect was also noticeable in the total cross sections of Figs. 5 and 6.

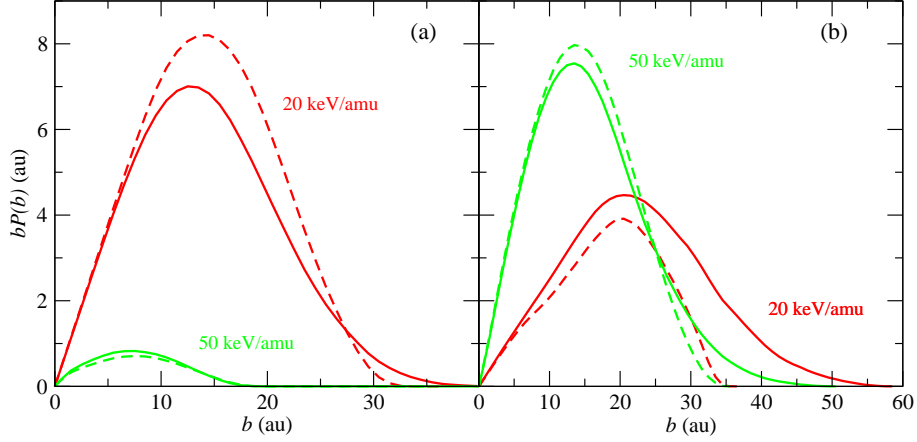


**Fig. 7.** Classical charge exchange (a) and ionization (b) opacity functions  $bP(b)$ , as functions of the impact parameter  $b$  for  $C^{6+} + H(n=2)$  collisions at  $E=20$  keV/amu and 50 keV/amu, obtained using hydrogenic (—) and microcanonical (- -) initial distributions.

**Table 1.** The most populated  $n$  level after each CX reaction as a function of the impact energy.

$E(\text{keV/amu})$	$C^{6+} + H(1s)$	$N^{7+} + H(1s)$	$C^{6+} + H(n=2)$	$N^{7+} + H(n=2)$
10	5	5	8	9
15	4	5	8	9
65	4	5	7	8
100	4	5	6	7
125	4	4	6	6
150	4	4	5	6
200	4	4	4	5

We observe in Figs. 8 and 9 a population distribution of the exit channels that depends on the initial state of the target. In order to study this point in more detail, we show in table 1 the most populated  $n$  level,  $n_{\text{max}}$ , after the electron capture for a wide range of impact energies. In the case of collisions with  $H(1s)$ ,  $n_{\text{max}} = 4$ , while  $n_{\text{max}}$  exhibits a wide variation with  $E$  for collisions with  $H(n=2)$ .

Previous works [42, 56, 57] have dealt with the probability of population for  $nl$  states in  $A^{(q-1)+*}(n, l)$  in the CX process. In particular, the classical over barrier model of [57] predicts  $n_{\text{max}} = 4, 9$  for  $C^{6+} + H(1s)$ ,  $H(n=2)$  collisions respectively, and  $n_{\text{max}} = 5, 10$  for  $N^{7+} + H(1s)$ ,  $H(n=2)$ , which qualitatively agree with our low-energy results. Olson [42], deduced from his CTMC calculations the simple relationship:

$$n_{\text{max}} \simeq n_i(q_f/q_i)^{3/4} \quad (9)$$

being  $n_i$  the principal quantum number of the electron in the target and  $q_f, q_i$ , the nuclear charges of projectile and target respectively. Our results for collisions with  $H(1s)$  qualitatively agree with (9). However, equation (9) leads to an energy independent  $n_{\text{max}}$  in contrast with our results for collisions with  $H(n=2)$  (see table 1).

In order to further illustrate the energy dependence of the CX into specific  $n$  levels, we display in Fig. 10 our hydrogenic-CTMC opacity functions,  $bP_n(b)$  ( $n = 4 - 9$ ), for  $C^{6+} + H(1s, n = 2)$  collisions. We first note that the

transition probabilities at  $E = 25$  keV/amu reflect the low-energy electron capture mechanism, which involves the polarization and subsequent delocalization of the electronic cloud, so that the capture takes place at large internuclear distances compared with the sizes of the initial radial distributions. At low energies, the relative populations of the atomic levels are determined by their energies, being the most populated ones those with energies close to that of the entrance channel. As  $E$  increases, the polarization of the electronic cloud becomes less important and the CX process takes place in a narrow range of impact parameters; this suggests that the reaction occurs via a binary encounter mechanism. In the particular case of collisions with  $H(n=2)$ , the dominant channels at low  $E$  are diffuse orbitals, populated at large  $b$ , and these populations decrease when the efficiency of the low-energy mechanism diminishes. This effect leads to the variation of  $n_{\text{max}}$  with  $E$  shown in table 1.

### 3.4 Partial $nl$ -resolved cross sections

We apply again the BM [48] binning (see equation (7)) to evaluate  $l$ -resolved partial charge exchange cross sections. As an illustration, we plot in Figs. 11 and 12 our results for  $C^{6+} + H$  at two collision energies, which have been selected for the importance of the capture process. For collisions with  $H(1s)$ , and for both energies, the  $l$ -distributions



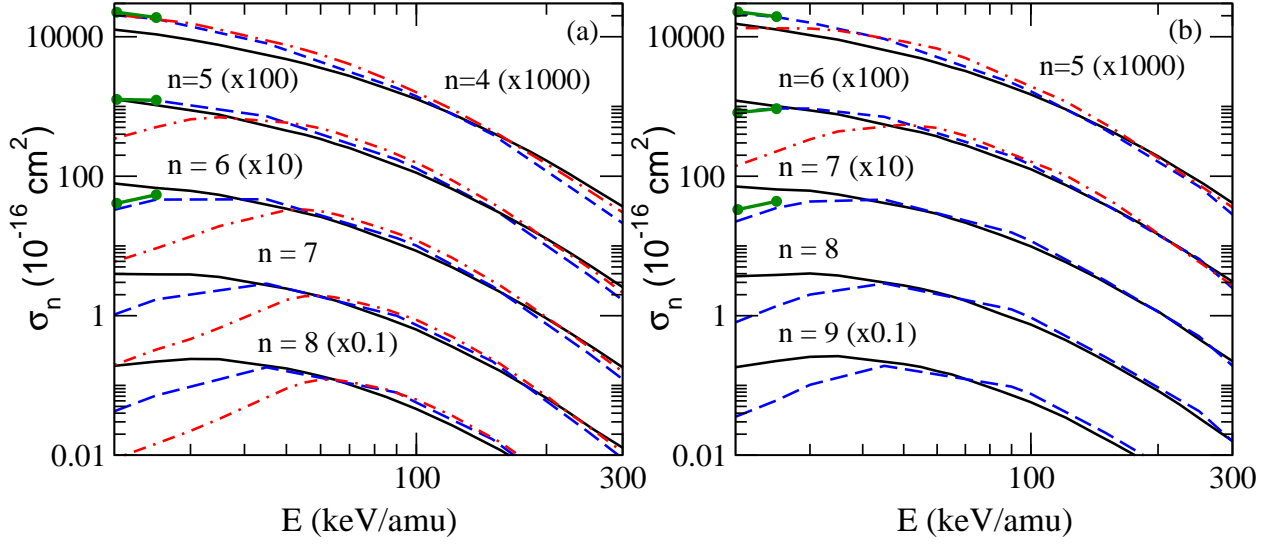


**Fig. 8.** Partial  $n$ -resolved CX cross sections for  $C^{6+}+H(1s)$  (a) and  $N^{7+}+H(1s)$  collisions (b): (—) hydrogenic-CTMC; (---) microcanonical-CTMC; (---) AOCC [21]; (●—●) MOCC [19].

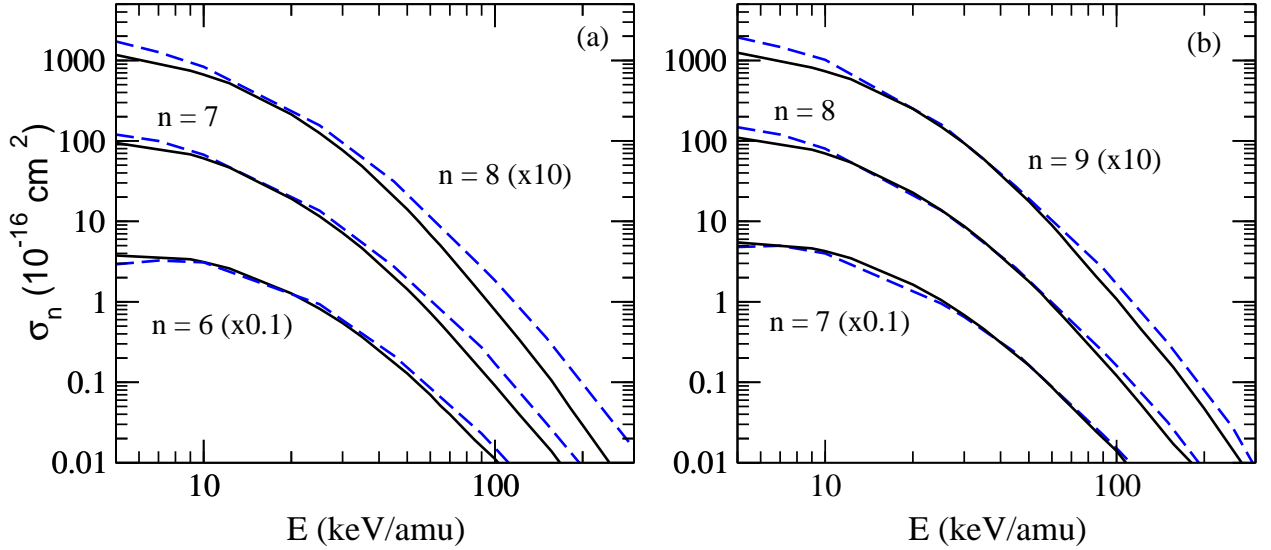


**Fig. 9.** Partial  $n$ -resolved CX cross sections for  $C^{6+}+H(n=2)$  (a) and  $N^{7+}+H(n=2)$  collisions (b): (—) hydrogenic-CTMC and (---) AOCC results [21].

of Fig. 11 show maxima at  $l_{\max} \approx 4$ , close to the value of  $n_{\max}$  of table 1. On the other hand, for collisions with  $H(n=2)$ , we have noted a strong dependence of  $n_{\max}$  on the impact energy (see table 1), which is also found for  $l_{\max}$ . At low collision energies ( $E = 25$  keV/amu), we find  $l_{\max} = n_{\max} - 1$ , while for  $E = 100$  keV/amu, where  $n_{\max} = 6$ , we obtain  $l_{\max} \approx q_f^{3/4}$ , as suggested in [42,58]. The decrease of population as  $l$  increases at high  $E$ , can be explained by using the classical argument of Olson [42]: The charge exchange process takes place when the electron approaches the projectile nucleus in collisions with relatively large  $b$  (see Fig. 10), which is only possible for highly eccentric (low  $l$ ) electron trajectories; this decrease is however not observed for the collisions with  $H(n=2)$

at  $E = 25$  keV/amu, where transitions take place at large internuclear separations for trajectories with large  $l$ , as a consequence of the charge exchange mechanism at low  $E$  explained in previous subsection.

In general, our  $nl$ -resolved cross sections agree with the AOCC ones [21], and, in particular, for the reaction with  $H(n=2)$ , the agreement between both calculations extends to low energies,  $E = 25$  keV/amu, as can be noted in Fig. 12 and it has previously shown for the  $n$ -partial cross sections in Fig. 8.



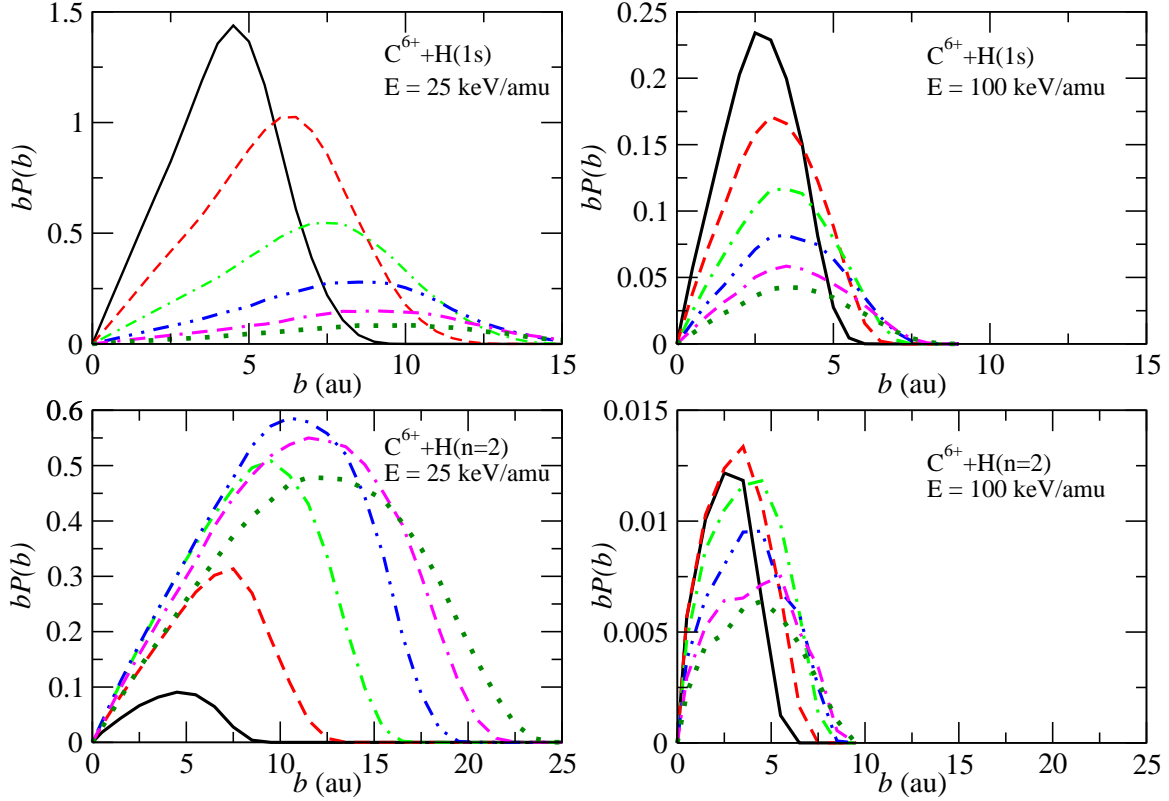


**Fig. 10.**  $bP_n(b)$  as a function of  $b$  for  $C^{6+} + H(1s)$  and  $H(n=2)$  at 25 and 100 keV/amu: (—)  $n=4$ ; (—)  $n=5$ ; (· · ·)  $n=6$ ; (· · ·)  $n=7$ ; (· · ·)  $n=8$ ; (· · ·)  $n=9$

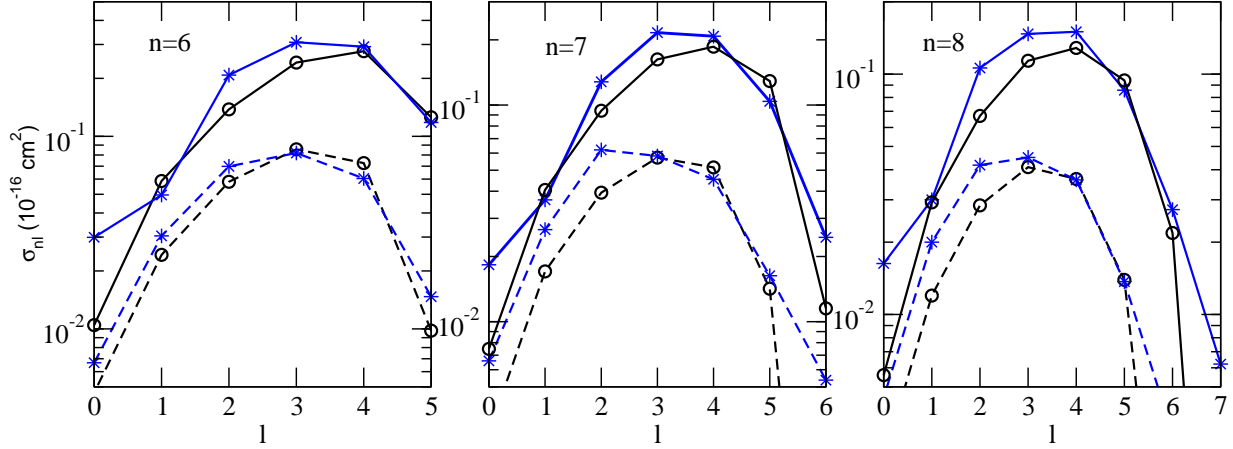


**Fig. 11.** Partial  $nl$ -resolved CX cross sections as functions of the quantum number  $l$ , for the collisions  $C^{6+} + H(1s)$ : Full lines:  $E = 100$  keV/amu; dashed lines:  $E = 150$  keV/amu. (○ — ○) hydrogenic-CTMC and (\* — \*) AOCC [21] results.

### 3.5 Scaling laws

One of the main aims of calculating charge exchange cross sections for intermediate- $Z$  projectiles is to be able to extrapolate the computed results to high  $Z$ -elements. The lack of data when considering collisions involving different high- $Z$  ions, especially for collisions with excited hydrogen, makes necessary the construction of reliable scaling laws. These scaling laws have to provide accurate charge

exchange cross sections by taking only into account the collision parameters, such as the impact velocity, the charge of the ion and the target state. In this respect, Foster [9] has used the cross sections, calculated or measured by different authors and, stored in ADAS for  $Z \leq 18$ , and has constructed the following scaling law for the total capture cross sections:

$$\sigma^* = \sigma Z^{-\alpha} \quad (10)$$

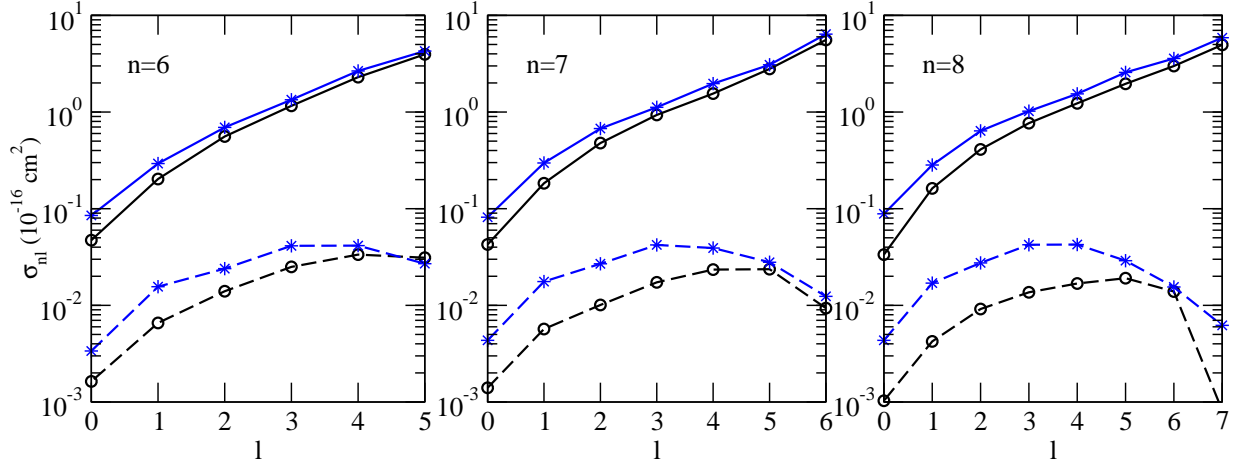


**Fig. 12.** Partial  $nl$ -resolved CX cross sections as functions of the quantum number  $l$ , for the collisions  $C^{6+} + H(n=2)$ : Full lines:  $E = 25$  keV/amu; dashed lines:  $E = 100$  keV/amu. ( $\circ - \circ$ ) hydrogenic-CTMC and ( $* - *$ ) AOCC [21] results.

with:

$$E^* = EZ^{-\beta} \quad (11)$$

and  $\alpha = 1.05$ ,  $\beta = 0.3$ .

In Fig. 13 we have plotted the present hydrogenic CTMC total CX cross sections for  $C^{6+}$  and  $N^{7+}$  projectiles colliding with ground-state and excited hydrogen atoms, together with those for  $Li^{3+}$  and  $Ne^{10+} + H(1s)$  [30] and for  $Ar^{18+} + H(1s)$  collisions [31], obtained with a similar approximation. We can observe a correct behaviour of the scaling law suggested by Foster [9].

Foster also proposed a scaling law for the  $n$ -partial cross sections:

$$\sigma_n^* = \sigma_n Z^{-\delta(E, n_i)} \quad (12)$$

$$n^* = n Z^{-\gamma(E, n_i)}, \quad (13)$$

where the parameters  $\delta$  and  $\gamma$  depend on the collision energy and the initial target state,  $n_i$ . In order to further check the validity of these scaling laws, we have considered the partial cross sections for  $C^{6+}$  and  $N^{7+} + H(1s)$  calculated in this work, previous results for  $Li^{3+}$ ,  $Ne^{10+}$ ,  $Ar^{18+} + H(1s)$  collisions, and we have calculated the partial cross sections for collisions of  $Li^{3+}$ ,  $Ne^{10+}$  and  $Ar^{18+} + H(n=2)$  at  $E = 50, 100$  keV/amu.

In the energy range of interest in fusion research (25-300 keV/amu), we have found that the optimal values of these parameters fulfill

$$\begin{aligned} \delta(E, n_i = 1) &= 1.54 - \frac{38.3}{E} + 1.80 \times 10^{-4} E \\ \delta(E, n_i = 2) &= 2.05 - \frac{22.5}{E} - 2.10 \times 10^{-3} E \\ \gamma(E, n_i = 1) &= \gamma(E, n_i = 2) = 1.02 - \frac{5.37}{E} \end{aligned} \quad (14)$$

As an illustration of these scalings for  $H(1s)$  and  $H(n=2)$  targets, we show in Fig. 14 the scaled  $n$ -partial cross sections  $\sigma_n^*$  as functions of  $n^*$ , for the above-mentioned optimal parameters. From this comparisons, it is clear the

general validity of the universal scaling law originally proposed by Foster. However, one can note that the results for  $Ar^{18+}$  at  $E = 50$  keV/amu (Fig. 14(a)) agree with the other plotted in this figure near the maximum, but the agreement worsens as  $n^*$  increases. As explained in [31], the CX partial cross sections for  $Ar^{18+} + H(1s)$  do not show the  $n^{-3}$  decay for  $E < 70$  keV/amu, exhibited by the other projectiles at  $E = 50$  keV/amu. In general, the scaling of eqs. (12)-(13) is not useful as the ratio  $Z/E$  increases. On the other hand, for collisions with  $H(n=2)$  (Fig. 14(b)), the partial cross sections are correctly reproduced by the scaling law for the five projectiles considered at energies above 25 keV/amu.

## 4 Summary

We have calculated total and partial cross sections for charge exchange and total ionization cross sections for  $C^{6+}$  and  $N^{7+} + H(n=1,2)$  collisions in the intermediate energy range  $5 \leq E \leq 500$  keV/amu. We have employed an impact parameter CTMC treatment and we have used two initial distributions, the standard microcanonical and the so-called hydrogenic one, whose spatial and momentum densities lie close to the quantal ones [23]. Although CX cross sections for ion collisions with  $H(n=2)$  are required in the CXRS diagnostics, few works have considered collisions with excited hydrogen.

In this work, we have ascertained that the microcanonical - CTMC calculations for collisions with  $H(1s)$  show important limitations at low impact energies in evaluating ionization and CX total cross sections. Moreover, this distribution is not appropriate for calculating state-selective cross sections for CX into highly excited states of the product ions, which are particularly relevant in CXRS. However, both initial distributions yield very similar results for collisions with  $H(n=2)$ , as a consequence of the relatively good description of quantal electron distribution by the microcanonical distribution of the excited states.

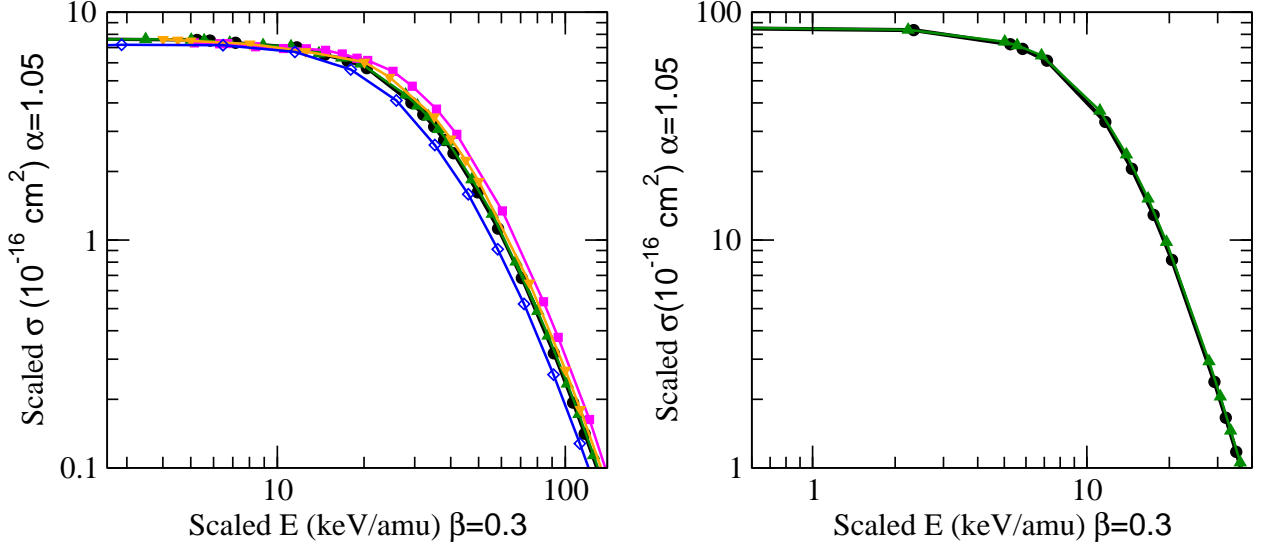


**Fig. 13.** Scaled total cross sections [9], for  $\text{Li}^{3+}$  ( $\diamond$ — $\diamond$ ) [30],  $\text{C}^{6+}$  ( $\bullet$ — $\bullet$ ),  $\text{N}^{7+}$  ( $\triangle$ — $\triangle$ ),  $\text{Ne}^{10+}$  ( $\nabla$ — $\nabla$ ) [30] and  $\text{Ar}^{18+}$  ( $\blacksquare$ — $\blacksquare$ ) [31] + H(1s) (left panel) and  $\text{C}^{6+}$ ,  $\text{N}^{7+}$  + H(n=2) (right panel) collisions.

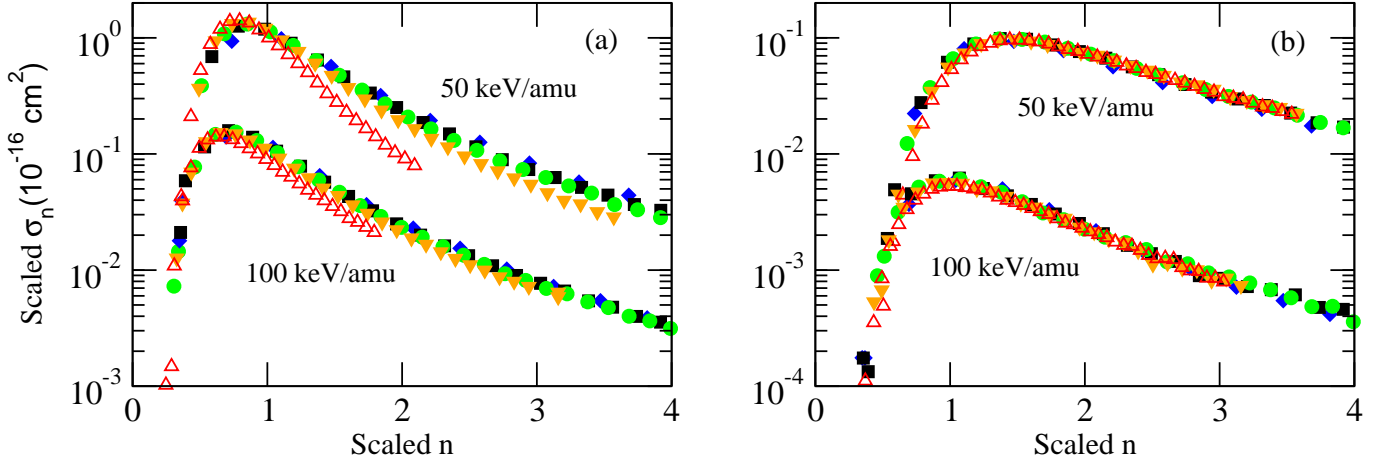


**Fig. 14.** Scaled  $n$ -partial cross sections [9], for  $\text{Li}^{3+}$  ( $\diamond$ ),  $\text{C}^{6+}$  ( $\blacksquare$ ),  $\text{N}^{7+}$  ( $\bullet$ ),  $\text{Ne}^{10+}$  ( $\nabla$ ) and  $\text{Ar}^{18+}$  ( $\triangle$ ) with H(1s) (a) and H(n=2) (b) collisions.

Our total hydrogenic-CTMC charge exchange cross sections show general good agreement with recent AOCC results by Igenbergs *et al.* [21] for the four studied systems while ionization cross sections for collisions with H(1s) targets show a better agreement with the AOCC results from Toshima [20]. With respect to the  $n$ -partial cross sections for collisions with H(1s) and the  $n$  levels relevant to fusion diagnostics, we find an excellent agreement with those of reference [21] at collision energies  $E > 40$  keV/amu. On the other hand, at energies lower than 40 keV/amu, where a better description of the semiclassical calculation is expected, the hydrogenic-CTMC calculations do not accurately reproduce the maxima of the partial cross sections. As the collision energy increases, the partial CX cross sections for collisions with H(n=2) fall much more rapidly than the corresponding ones for ion-H(1s) collisions, and

the hydrogenic-CTMC and AOCC [21]  $n$ -partial cross sections present a good agreement from  $E \gtrsim 10$  keV/amu.

A set of recommended data for these two systems will involve the smooth joining of CTMC and AOCC cross sections and, in general, the use of the AOCC cross sections for CX into low- $n$  final states is recommended. The quality of the CTMC partial CX cross sections improves as  $n$  increases and it is the only method applicable to calculate them for high-lying  $n$  final states and to simultaneously evaluate ionization cross sections. In this respect, the ADAS database contains CX cross sections for  $\text{C}^{6+}$  + H(n=1, 2) collisions that should be updated using the present results and those of reference [21]. The situation is worse for  $\text{N}^{7+}$  + H(n=1, 2) collisions, where only interpolated data are stored because of the lack of previous calculations. Finally, we have checked that our CTMC results can be accurately fitted by means of the universal

scaling law of Foster [9] and we give the optimal parameters for collisions with  $H(1s)$  and  $H(n=2)$  targets.

This work has been supported by the projects ENE2007-62934 and ENE2011-28200 of the Secretaría de Estado de Investigación, Desarrollo e Innovación (Spain), and the ADAS-EU Euratom Framework 7 Support Action.

## References

1. H.P. Summers (Academic Press, 1994), Vol. 33 of *Advances In Atomic, Molecular, and Optical Physics*, p. 275
2. R.C. Isler, Plasma Phys. Control. Fusion **36**, 171 (1994)
3. D.M. Thomas, Phys. Plasmas **19**, 056118 (2012)
4. H. Anderson, M.G. von Hellermann, R. Hoekstra, L.D. Horton, A.C. Howman, R.W.T. Konig, R. Martin, R.E. Olson, H.P. Summers, Plasma Phys. Control. Fusion **42**, 781 (2000)
5. H.P. Summers, *The ADAS User Manual 2.6* (2006)
6. Y. Ralchenko, I.N. Draganic, J.N. Tan, J.D. Gillaspay, J.M. Pomeroy, J. Reader, U. Feldman, G.E. Holland, J. Phys. B: At. Mol. Opt. Phys. **41**, 021003 (2008)
7. R.K. Janev, Phys. Lett. A **160**, 67 (1991)
8. K.R. Cornelius, K. Wojtkowski, R.E. Olson, J. Phys. B: At. Mol. Opt. Phys. **33**, 2017 (2000)
9. A. Foster, Ph.D. thesis, University of Strathclyde (2008)
10. C. Illescas, L.F. Errea, L. Mendez, Phys. Scr. **2013**(T156), 014033 (2013)
11. C.H. Skinner, Phys. Scr. **2009**(T134), 014022 (2009)
12. N. Asakura, T. Nakano, N. Oyama, T. Sakamoto, G. Matsunaga, K. Itami, Nucl. Fusion **49**, 115010 (2009)
13. A. Kallenbach, R. Dux, J.C. Fuchs, R. Fischer, B. Geiger, L. Giannone, A. Herrmann, T. Lunt, V. Mertens, R. McDermott et al., Plasma Phys. Control. Fusion **52**, 055002 (2010)
14. R.C. Isler, R.E. Olson, Phys. Rev. A **37**, 3399 (1988)
15. V.S. Lisitsa, L.A. Bureyeva, A.B. Kukushkin, M.B. Kadomtsev, V.A. Krupin, M.G. Levashova, A.A. Medvedev, E.E. Mukhin, V.A. Shurygin, S.N. Tugarinov et al., J. Phys.: Conf. Ser. **397**, 012015 (2012)
16. R. Hoekstra, H. Anderson, F.W. Blik, M. von Hellerman, C.F. Maggi, R.E. Olson, H.P. Summers, Plasma Phys. Control. Fusion **40**, 1541 (1998)
17. H.P. Summers, H. Anderson, M.G. O'Mullane, M.G. von Hellermann, Phys. Scr. **2001**(T92), 80 (2001)
18. S. Tugarinov, M. Kadomtsev, M. Levashova, V. Lisitsa, N. Nagel, 36th EPS Conference on Plasma Phys. ECA **33E** (2009)
19. C. Harel, H. Jouin, B. Pons, At. Data. Nucl. Data Tables **68**, 279 (1998)
20. N. Tushima, Phys. Rev. A **50**, 3940 (1994)
21. K. Igenbergs, J. Schweinzer, A. Veiter, L. Perneczky, E. Frühwirth, M. Wallerberger, R.E. Olson, F. Aumayr, J. Phys. B: At. Mol. Opt. Phys. **45**, 065203 (2012)
22. D.J.W. Hardie, R.E. Olson, J. Phys. B: At. Mol. Phys. **16**, 1983 (1983)
23. C. Illescas, A. Riera, Phys. Rev. A **A60**, 4546 (1999)
24. R.D. Rivarola, P.D. Fainstein, V.H. Ponce, Phys. Scr. **1989**(T28), 101 (1989)
25. D. Belkić, S. Saini, H.S. Taylor, Phys. Rev. A **36**, 1601 (1987)
26. M.S. Gravielle, J.E. Miraglia, Phys. Rev. A **51**, 2131 (1995)
27. A. Costley, T. Sugie, G. Vayakis, C. Walker, Fusion Engineering and Design **74**, 109 (2005)
28. R. Abrines, I.C. Percival, Proc. Phys. Soc. **88**, 861 (1966)
29. L.F. Errea, C. Illescas, L. Méndez, B. Pons, A. Riera, J. Suárez, Phys. Rev. A **70**, 52713 (2004)
30. L.F. Errea, C. Illescas, L. Méndez, B. Pons, A. Riera, J. Suárez, J. Phys. B: At. Mol. Opt. Phys. **37**, 4323 (2004)
31. L.F. Errea, C. Illescas, L. Méndez, B. Pons, A. Riera, J. Suarez, J. Phys. B: At. Mol. Opt. Phys. **39**, L91 (2006)
32. L.F. Errea, F. Guzmán, C. Illescas, L. Méndez, B. Pons, A. Riera, J. Suárez, Plasma Phys. Control. Fusion **48**, 1585 (2006)
33. F. Guzmán, L.F. Errea, C. Illescas, L. Méndez, B. Pons, J. Phys. B: At. Mol. Opt. Phys. **43**, 144007 (2010)
34. J. Suarez, F. Guzmán, B. Pons, L.F. Errea, J. Phys. B: At. Mol. Opt. Phys. **46**, 095701 (2013)
35. S. Otranto, Journal of Physics: Conference Series **388**, 012035 (2012)
36. I. Blank, S. Otranto, C. Meinema, R.E. Olson, R. Hoekstra, Phys. Rev. A **85**, 022712 (2012)
37. W. Mandl, R.C. Wolf, M.G. von Hellermann, H.P. Summers, Plasma Phys. Control. Fusion **35**, 1373 (1993)
38. R.K. Janev, C.D. Boley, D.E. Post, Nucl. Fusion **29**, 2125 (1989)
39. A. Jorge, L.F. Errea, C. Illescas, L. Méndez, J. Suarez, Phys. Scr. **2013**(T156), 014032 (2013)
40. B.H. Bransden, M.H.C. McDowell, *Charge Exchange and the Theory of Ion-Atom Collisions* (Oxford, Clarendon, 1992)
41. R. Olson, A. Salop, Phys. Rev. A **16**, 631 (1977)
42. R.E. Olson, Phys. Rev. A **24**, 1726 (1981)
43. C. Illescas, I. Rabadán, A. Riera, J. Phys. B: At. Mol. Opt. Phys. **30**, 1765 (1997)
44. J.S. Cohen, J. Phys. B: At. Mol. Opt. Phys. **18**, 1759 (1985)
45. M.J. Raković, D.R. Schultz, P.C. Stancil, R.K. Janev, J. Phys. A: Math. Gen. **34**, 4753 (2001)
46. C. Illescas, I. Rabadán, A. Riera, Phys. Rev. A **57**, 1809 (1998)
47. E.Y. Sidky, C. Illescas, C.D. Lin, Phys. Rev. Lett. **85**, 1634 (2000)
48. R.L. Becker, A.D. MacKellar, J. Phys. B: At. Mol. Phys. **17**, 3923 (1984)
49. F.W. Meyer, A.M. Howald, C.C. Havener, R.A. Phaneuf, Phys. Rev. A **32**, 3310 (1985)
50. T.V. Goffe, M.B. Shah, H.B. Gilbody, J. Phys. B: At. Mol. Opt. Phys. **12**, 3763 (1979)
51. W. Fritsch, C.D. Lin, J. Phys. B: At. Mol. Phys. **17**, 3271 (1984)
52. W. Fritsch, C.D. Lin, Phys. Rep. **202**, 1 (1991)
53. H. Ryufuku, Phys. Rev. A **25**, 720 (1982)
54. C. Illescas, A. Riera, J. Phys. B: At. Mol. Opt. Phys. **31**, 2777 (1998)
55. C. Illescas, B. Pons, A. Riera, Phys. Rev. A **63**, 062722 (2001)
56. H. Ryufuku, T. Watanabe, Phys. Rev. A **20**, 1828 (1979)
57. H. Ryufuku, K. Sasaki, T. Watanabe, Phys. Rev. A **21**, 745 (1980)
58. D.R. Schultz, P.C. Stancil, M.J. Rakovic, J. Phys. B: At. Mol. Opt. Phys. **34**, 2739 (2001)